Tapped-Inductor-Based Single-Magnetic Bidirectional PWM Converter Integrating Cell Voltage Equalizer for Series-Connected Supercapacitors

Masatoshi Uno, *Member*, *IEEE*, Kazuki Yashiro

***Abstract*—Conventional supercapacitor (SC)-based energy storage systems require two separate converters, namely a bidirectional converter and cell voltage equalizer. Each converter requires magnetic components, hence increasing the complexity, volume, and cost. This paper proposes the single-magnetic bidirectional converter integrating a cell voltage equalizer. The proposed integrated converter is derived from the combination of a bidirectional PWM converter with a tapped-inductor (TI) and a resonant voltage multiplier (RVM). The RVM is driven by the TI generating a square wave voltage with an arbitrary amplitude. Not only is the system simplified by the integration but also the single-magnetic topology achieves circuit miniaturization. A 100-W prototype for nine SCs connected in series was built for the experimental charge-discharge cycling test. The voltage mismatch of SCs automatically disappeared during charge-discharge cycling, demonstrating the integrated functions of the proposed converter.**

***Keywords*—Integration, PWM converter, supercapacitors, tapped inductor, voltage equalizer.**

NOMENCLATURE

A_C	Cross-sectional area of core [cm^2]
B_{pp}	Peak-to-peak flux density [T]
B_{max}	Maximum flux density [T]
C_r	Resonant capacitance [F]
d	Duty cycle of high-side switch Q_H
f_s	Switching frequency [Hz]
f_r	Resonant period [Hz]
i_{Cr}	Current of resonant capacitor C_r [A]
I_{bus}	Bus current [A]
I_{string}	String current [A]
I_{eq}	Equalization current [A]
i_{Lkg}	Current of leakage inductance L_{kg} [A]
I_{Lkg}	Average current of leakage inductance L_{kg} [A]
i_{Lmg}	Current of magnetizing inductance L_{mg} [A]
I_{Lmg}	Average current of magnetizing inductance L_{mg} [A]
I_P, I_S	Primary and secondary winding current [A]
I_{VM}	Average of rectified i_{Cr} [A]
K_L, K_{Tr}	Coefficient
l_g	Gap length of core [m]
L_{eq}	Equivalent inductance of TI [H]
L_{kg}	Leakage inductance of TI [H]
L_{mg}	Magnetizing inductance of TI [H]
n	Number of cells connected in series
N	Turn ratio of TI
N_P, N_S	Number of turns of primary and secondary windings
R	Collective resistance in resonant current path [Ω]
R_{eq}	Equivalent resistance of coupling capacitor [Ω]
S_{tot}	Total volt-amp rating of windings
T_S	Switching period [s]
V_{bias}	Voltage of bias resistor R_{bias} [V]
V_{bus}	Bus voltage [V]
v_{Cr}	Voltage of resonant capacitor C_r [V]
$V_{Cr.ave}$	Average of v_{Cr} [V]
$V_{Cr.j}$	v_{Cr} at the beginning of j-th mode [V]
V_F	Diode forward voltage drop [V]
V_i	Least charged cell voltage [V]
v_L	Voltage across TI [V]
V_{PP_TI}	Peak-to-peak voltage of v_{TI} [V]
V_{Rvar}	Voltage of variable resistor R_{var} [V]
V_{string}	String voltage [V]
v_{TI}	Ground-referenced center-tap voltage of TI [V]
$V_{TI.j}$	Average v_{TI} in j-th mode [V]
v_{VM}	Input voltage of voltage multiplier [V]
$V_{VM.even}$	V_{VM} during even-numbered diodes are on [V]
$V_{VM.j}$	Average v_{VM} in j-th mode [V]
$V_{VM.odd}$	V_{VM} during odd-numbered diodes are on [V]
Z_0	Characteristic impedance [Ω]
$\alpha_{ch.L}$	Largest dimension of inductor [cm]
$\alpha_{ch.Tr}$	Largest dimension of transformer [cm]
β	Ripple factor
γ	Damping factor
ΔI_{Lmg}	Ripple current component of I_{Lmg} [A]
ΔV_C	Voltage variation of C [V]
η_{RVM}	Power conversion efficiency of RVM
η_{whole}	Power conversion efficiency of integrated converter
λ	Exponent characterizing core material and shape
μ_0	Magnetic permeability [H/m]
ω_r	Characteristic angular frequency [rad/s]
ω_0	Resonant angular frequency [rad/s]
ω_S	Angular switching frequency [rad/s]

M. Uno is with the College of Engineering, Ibaraki University, Hitachi 316-8511, Japan (e-mail: masatoshi.uno.ee@vc.ibaraki.ac.jp).

K. Yashiro is with the Nippon Chemi-Con Corporation, Shinagawa 141-8605, Japan (e-mail: yashi@nippon.chemi-con.co.jp).

I. INTRODUCTION

The role of energy storage systems based on rechargeable batteries has increasingly become important in various applications, including electric vehicles and renewable energy systems, such as photovoltaic and wind turbine systems. At the same time, applications of supercapacitors (SCs) are also rapidly expanding. SCs have been chiefly used in hybrid power systems where they are used as a high-power energy buffer. To adopt SCs in such hybrid energy storage systems for electric vehicles and renewable energy applications, a variety of studies, such as dynamic behavior modeling [1], [2], evaluation of cycle life performance [3], [4], control systems [5]–[7], and optimal sizing [8], [9], have been underway.

SCs are also gaining popularity as an alternative energy storage source to traditional rechargeable batteries [10]–[12] because of their excellent long service life. In uninterruptible power supply (UPS) applications, for example, SCs' long-life performance realizes maintenance-free operations—battery replacement is mandatory for every few years in traditional UPSs using lead-acid batteries.

Since a typical voltage range of a single SC cell is 0–3.0 V, multiple cells need to be connected in series to form a module and to meet the voltage requirement of systems or loads. Voltages of series-connected cells gradually become imbalanced because of minor mismatches in cell characteristics, such as capacitance, self-discharge rate, degradation rate, and internal impedance. The temperature distribution is also a major cause of voltage imbalance as the self-discharge rate is significantly dependent on temperature—the higher the temperature, the faster will be the self-discharging. In a voltage-mismatched module, some cells with higher voltage might be over-charged during charging, accelerating the irreversible degradation and increasing the risk of hazardous consequences. Furthermore, since a degradation rate of SC cells is dependent on voltage—the higher the voltage, the faster will be the aging—, cells in a voltage-mismatched module unevenly deteriorate, resulting in accelerated aging of the module as a whole. Thus, voltages of series-connected cells need to be balanced to ensure years of safe operation of SCs.

Various kinds of voltage equalizers and equalization architectures have been proposed and developed [13]–[35]. With equalizers, energies of cells with higher voltage are transferred to cells with lower voltage so that all cell voltages are eventually unified. Adjacent cell-to-cell equalizers based on bidirectional converters, such as PWM converters [13]–[16] and switched capacitor converters [17]–[23], are the most straightforward approach to equalize cell voltages. But this equalization architecture requires $n - 1$ equalizers for n cells, hence increasing the system complexity. Another drawback of the adjacent cell-to-cell equalizers is that the power transfer is limited only between adjacent two cells, and therefore, energies may have to traverse multiple cells and equalizers before reaching target cells, collectively increasing the power conversion loss during equalization.

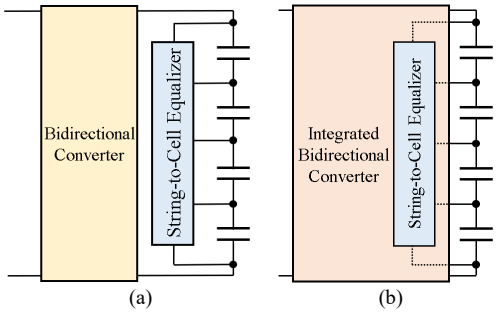

Fig. 1. Energy storage systems using (a) string-to-cell equalizer and (b) integrated converter.

Direct cell-to-cell equalization architectures using selection switches have been proposed [24]–[27]. In addition to the direct energy transfer to target cells, the number of converters necessary can be drastically reduced. Equalization algorithms, however, are prone to be complex as voltage measurement, comparison, and calculation are indispensable to determine target cells. Furthermore, since the number of bidirectional switches necessary is proportional to the cell count, circuit complexity tends to increase as each switch requires a gate driver and gating signal from a microcontroller. These equalizers are considered best suitable for large-scale systems where relatively complex circuits and control algorithms are acceptable to maximize the performance and minimize the size.

String-to-cell equalizers achieve direct energy-transfer from a string to cells via a single power-conversion stage [28]–[35]. The string-to-cell equalizers are essentially a single-input–multi-output converter, and the switch count of these equalizers can be a few, dramatically reducing the circuit complexity compared to other types of equalizers. In addition to the simple circuit, direct power transfer from the string to the least charged cell is feasible even without voltage measurement nor feedback control loop. These equalizers are very suitable for small- to medium-scale energy storage systems because of the simple circuit and lack of complex equalization algorithms or control circuit.

The energy storage system employing the string-to-cell equalizer is illustrated in Fig. 1(a). The string is charged-discharged by the bidirectional converter while the string-to-cell equalizer unifies cell voltages. Two separate converters are necessary for this system, indicating that there is room for improvement. By integrating these two converters into a single unit, the system can be further simplified, as depicted in Fig. 1(b).

The bidirectional PWM converter integrating a voltage equalizer based on the resonant voltage multiplier (RVM) has been proposed [36], as shown in Fig. 2. The RVM plays a role of voltage equalization. The square wave voltage at the switching node is utilized to drive the equalizer, and hence, the equalizer itself is essentially switchless. Although the bidirectional converter and equalizer can be integrated, this integrated converter requires two separate magnetic components (an inductor for the bidirectional converter and

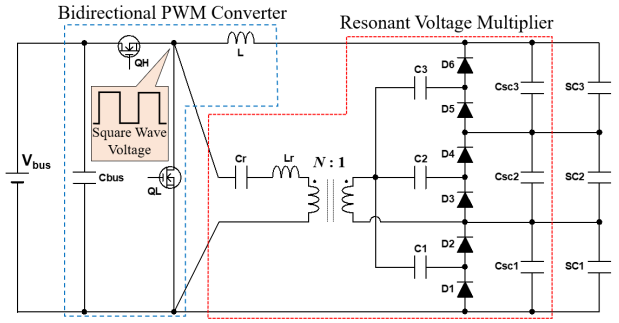

Fig. 2. Conventional bidirectional PWM converter integrating cell voltage equalizer based on resonant voltage multiplier (RVM) [34].

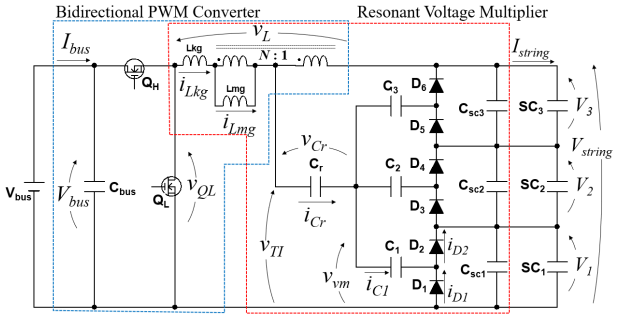

Fig. 3. Proposed tapped-inductor-based single-magnetic bidirectional PWM converter integrating cell voltage equalizer.

transformer for the RVM). It suggests that the integrated converter can simplify the system and circuit but is not beneficial from the viewpoint of circuit volume.

This paper proposes the tapped inductor-based single-magnetic bidirectional PWM converter integrating a voltage equalizer for series-connected SCs, as shown in Fig. 3. The tapped inductor (TI) plays three roles in the proposed integrated converter. The magnetizing and leakage inductances are utilized as a filter inductor and resonant inductor, respectively. Meanwhile, the TI can generate a square wave voltage with an arbitrary amplitude that is determined by its turn ratio. The RVM is driven by the square wave voltage generated by the TI.

The rest of this paper is organized as follows. Section II details the circuit description and major features of the proposed integrated converter. Section III performs operation analysis, followed by a design example of the TI in Section IV. Section V discusses the comparison with conventional magnetic integration technique and integrated converter. A dc equivalent circuit is derived, and its simulation results are presented in Section VI. Section VII shows the experimental results of a charge-discharge cycling test using the prototype for nine SCs connected in series.

II. Tapped Inductor-Based Bidirectional PWM Converter Integrating Resonant Voltage Equalizer

A. Circuit Description

The proposed integrated converter is derived from the combination of the bidirectional PWM converter and RVM. The bidirectional PWM converter works as a charge-discharge regulator. Meanwhile, the RVM plays the role of cell voltage equalization. The resonant operation is incorporated in the VM to realize the constant output current characteristic, not soft-switching operations—switches in the proposed converter are driven with a traditional hard switching manner. The constant output current characteristic of the RVM will be formulated in Section III-D.

The proposed integrated converter for three SCs, SC_1–SC_3, connected in series is shown in Fig. 3, as an example. In practical use, the proposed integrated converter and SCs are connected using cables, and currents from the converter should be sufficiently smoothed by eliminating ac current components. To decouple ac currents flowing in the RVM, smoothing capacitors C_{SC1}–C_{SC3} are connected in parallel with SC_1–SC_3, respectively. The series connection of C_{SC1}–C_{SC3} is connected in parallel with the string and, therefore, also behaves as a smoothing capacitor for the string.

A filter inductor in an ordinary bidirectional converter is replaced with the TI having a turn ratio of N:1, and TI's magnetizing inductance L_{mg} is utilized as the filter inductor. The center tap of the TI is tied to the input of the RVM, and TI's leakage inductance L_{kg} functions as a resonant inductor. During operation, a square wave voltage with a peak-to-peak value of V_{bus}–V_{string} appears across the TI and is divided by N+1. In other words, the TI behaves as a voltage divider. The ground-referenced center-tap voltage v_{TI} is applied to the RVM. The input voltage amplitude of the RVM can be arbitrarily chosen by properly adjusting the turn ratio N of the TI. In summary, the TI plays three roles of the filter inductor, resonant inductor, and voltage divider—unlike traditional autotransformers, a non-isolated transformer used for voltage conversion (or voltage division), the magnetizing and leakage inductances are also purposefully used for the TI in the proposed integrated converter. The detailed discussion and explanation will be presented in Section III.

The PWM converter controls the string current I_{string} and voltage V_{string} during charging while the RVM equalizes cell voltages. During discharging, the PWM converter regulates the bus voltage V_{bus}, and the RVM keeps equalizing cell voltages. Even without feedback control nor voltage measurement during both charging and discharging, the equalization current automatically flows toward the least charged cell(s) in the string. In other words, controlling the bidirectional PWM converter simply achieves not only bidirectional power conversion but also voltage equalization. The mechanism of the automatic voltage equalization can be found in the previous work [36].

The number of SCs connected in series can be arbitrarily extended by adding diodes, coupling capacitors (C_1–C_n), and smoothing capacitors (C_{SC1}–C_{SCn}) in the RVM for n cells connected in series, as shown in Fig. 4. Since the resonant capacitor C_r and C_1–C_n are connected in series in the RVM, the bias resistor R_{bias} is necessary in practical use to stabilize capacitor voltages—a bias current of a few milliamperes for R_{bias} would be large enough, similar to ordinary pull-up and -down resistors used for biasing. In the following sections, R_{bias}

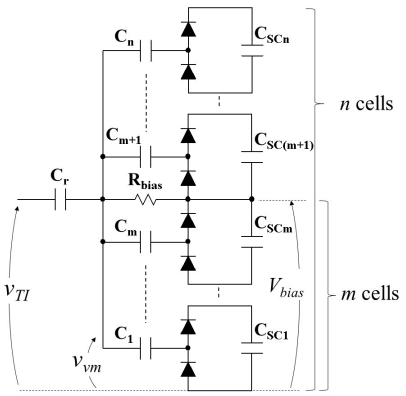

Fig. 4. Voltage multiplier for n cells connected in series.

is not illustrated for the sake of clarity.

B. Features

The obvious benefit of the integrated converter is the simplified system thanks to the reduced component count; the numbers of converters necessary are one and two in the proposed and conventional systems, respectively, as can be seen in Fig. 1. The most prominent feature of the proposed integrated converter is the single-magnetic topology. In general, magnetic components are the bulkiest element in power electronics circuits, and hence, the proposed converter contributes to reducing the circuit volume.

Since both the magnetizing and leakage inductances are purposefully utilized in the proposed integrated converter, the TI needs to be properly designed to realize desirable inductance values. Although it might be a design challenge, transformers conventionally used for LLC resonant converters [37] can be employed as a TI for the proposed integrated converter—LLC resonant converters utilize both magnetizing and leakage inductances to achieve frequency-dependent gain characteristics. In order for magnetizing and leakage inductances to be desirable values, transformers for LLC converters employ a gapped core and bobbin having separated compartments for primary and secondary windings.

The output currents of the RVM, or equalization currents supplied to cells, can be inherently constant even without feedback control as long as the RVM operates in discontinuous conduction mode (DCM), in which a current of the resonant tank becomes non-sinusoidal for certain periods. The constant current characteristic is an appealing feature for SCs that are essentially a voltage source. An SC with 0 V, for example, is equivalently a short-circuit load, and therefore, equalizers need to limit their output currents. With the RVM operating in the DCM, equalization currents for SCs are constant and automatically limited even without a feedback control loop, achieving the simplified circuit by eliminating feedback control for equalization currents.

III. Operation Analysis

Although the proposed integrated converter looks similar to the conventional one, mathematical equations presented in [36] cannot be directly applied because, in addition to C_r being directly connected to the VM, the RVM is driven by the square wave voltage divided by the TI. In this section, the operation modes of the original circuit (Fig. 3) are presented first in Section III-B, followed by the derivation and detailed modeling based on an equivalent circuit in Section III-D.

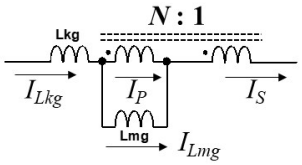

Fig. 5. Current relationship in tapped inductor.

The operation analysis is performed based on the premise that all circuit elements are ideal unless otherwise noted. Although this section deals with the case that the voltage of SC_1, V_1, is the lowest in the string, the converter's operation can be analyzed similarly in any other case. This section deals with only the charging mode, but the operation in the discharging mode can be analyzed similarly.

As explained in Section II-A, the bidirectional converter and RVM work as a charge-discharge regulator and cell voltage equalizer, respectively. Operation analyses for these two circuits are separately performed in Sections III-C and III-D for the sake of clarity.

A. Current Relationship in Tapped-Inductor

To grasp the relationship between i_{Lkg} and i_{Lmg} of the TI, ac current components are ignored, as shown in Fig. 5—i_{Cr} drawn from the center tap can be disregarded because a dc current of C_r is zero under steady-state conditions. The relationship between primary and secondary winding currents, I_P and I_S, is given by

$$I_S = -NI_P \tag{1}$$

In the practical use, the TI is connected in series with the string, and therefore, $I_{Lkg} = I_S = I_{string}$ under steady I_{Lkg} is equal to the sum of I_{Lmg} and I_P, yielding

$$I_{Lmg} = I_{Lkg} - I_P = \frac{N+1}{N} I_{Lkg} = \frac{N+1}{N} I_{string} \tag{2}$$

B. Operation Principle

Key operation waveforms and current flow directions are shown in Figs. 6 and 7, respectively. The waveforms are illustrated assuming $L_{mg} >> L_{kg}$, and the voltage across L_{kg} is negligibly small. Since the RVM operates in DCM, the current of the resonant tank, i_{Cr}, becomes non-sinusoidal in Modes 3 and 6.

Mode 1 ($T_0 \le t < T_1$): The high-side switch Q_H is turned on, and the magnetizing inductance current i_{Lmg} linearly increases. The input voltage of the RVM, v_{TI}, is equal to $(V_{bus}+NV_{string})/(N+1)$. The resonant capacitor C_r resonates with L_{kg}, and sinusoidal current i_{Cr} starts flowing in the RVM. i_{Cr} flows through the high-side diode D_2 and the coupling capacitor C_1. Mode 1 ends as i_{Cr} crosses zero.

Mode 2 ($T_1 \le t < T_2$): This operation mode is essentially identical to Mode 1, except for the current flow direction in the

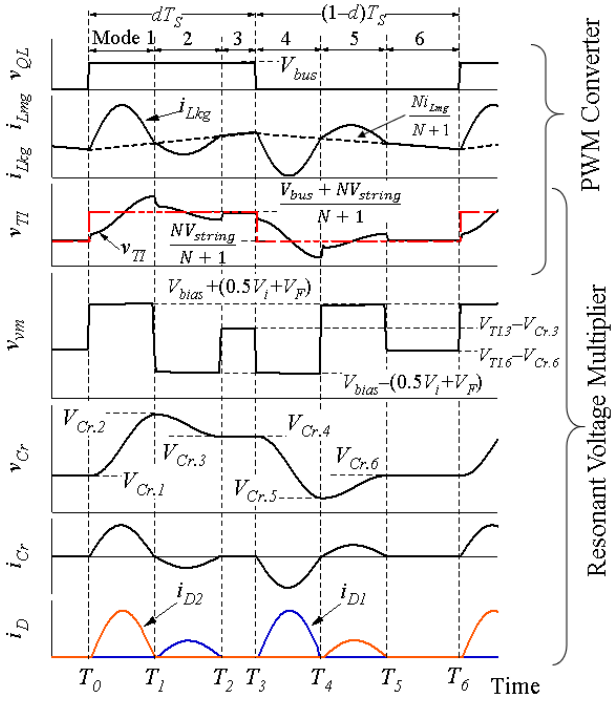

Fig. 6. Key operation waveforms when V_I is the lowest.

RVM. i_{Cr} is negative, and the low-side diode D_1 conducts. Mode 2 lasts until i_{Cr} reaches zero again.

Mode 3 ($T_2 \le t < T_3$): i_{Lmg} still linearly increases, similar to the previous two operation modes. No current flows in the RVM, and therefore, this operation mode is essentially identical to an on-period of traditional PWM buck converters.

Mode 4 ($T_3 \le t < T_4$): This mode begins as Q_H and Q_L are turned-off and -on, respectively. i_{Lmg} starts linearly decreasing, and v_{TI} becomes its low level of $NV_{string}/(N+1)$. C_r and L_{kg} start resonating again, and sinusoidal current i_{Cr} flows through C_1 and D_1. The operation moves to the next mode as i_{Cr} becomes zero.

Mode 5 ($T_4 \le t < T_5$): This operation mode is identical to Mode 4, except for current flow directions in the RVM. i_{Cr} is positive, and the high-side diode D_2 conducts.

Mode 6 ($T_5 \le t < T_6$): The RVM is inactive in this mode because all currents in the RVM are zero. Therefore, this operation mode is essentially equal to an off-period of ordinary PWM buck converters.

Overall, i_{Lmg} linearly increases and decreases, similar to traditional PWM buck converters. This suggests that the voltage conversion ratio of the proposed integrated converter is identical to traditional PWM buck converters. Meanwhile, as v_{TI} swings, resonant currents flow in the RVM. As long as the inactive periods of Modes 3 and 6 exist, one switching cycle contains two resonant periods, regardless of duty cycle variations. In other words, the operation of the RVM in unaffected by duty cycle variations of the bidirectional PWM converter.

C. Bidirectional PWM Converter

The voltage applied to the TI, v_L (designated in Fig. 3), in the on- and off-periods are $V_{bus}-V_{string}$ and $-V_{string}$, respectively. From the volt-sec balance on the TI, the voltage conversion ratio of the PWM converter is

$$V_{string} = dV_{bus} \tag{3}$$

where d is the duty cycle of Q_H.

In order to ensure DCM operations, Modes 3 and 6 need to exist, and the resonant period must be shorter than both dT_S and $(1-d)T_S$. The operation criterion of the integrated converter is given by

$$1-\frac{f_S}{f_r} > d > \frac{f_S}{f_r} \tag{4}$$

This equation suggests that if extreme duty cycle operations are expected, the resonant circuit should be designed so that f_r be extremely high compared to f_S. Since L_{kg} is not an arbitrarily adjustable parameter, C_r should be properly determined to

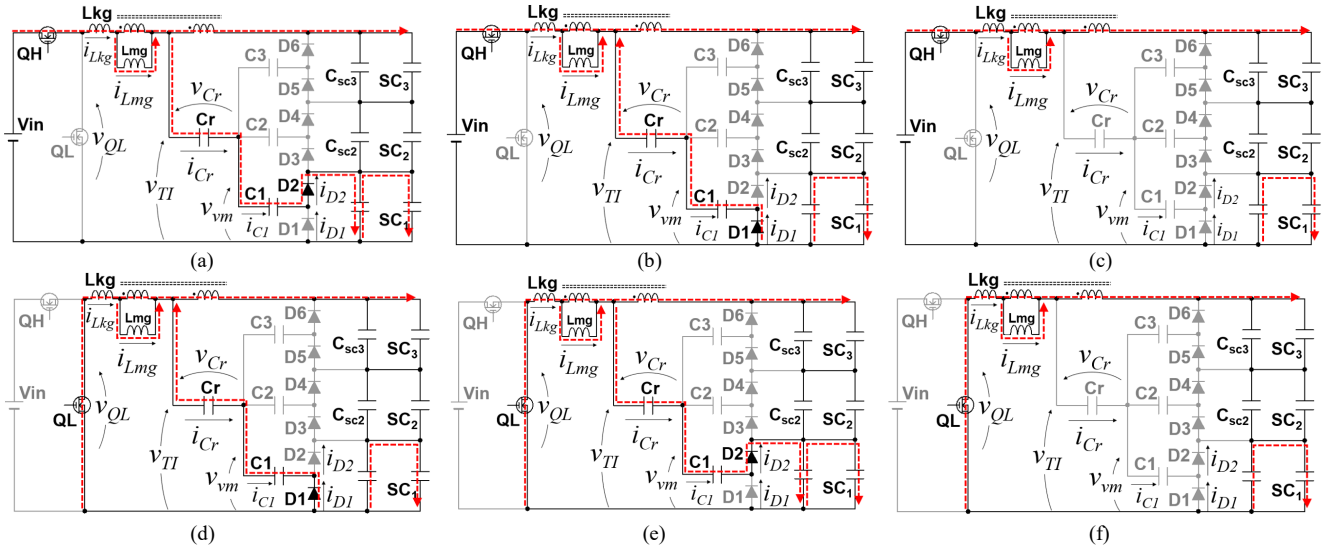

Fig. 7. Operation modes in battery charging mode. (a) Mode 1, (b) Mode 2, (c) Mode 3, (d) Mode 4, (e) Mode 5, (f) Mode 6.

substantiate the desired value of f_r based on (7).

D. Modeling of Resonant Voltage Multiplier (RVM)

In this subsection, an equivalent circuit of the RVM is derived, followed by the detailed analysis and modeling.

The rectangular wave voltage across the TI, v_L, is divided by $1/(N+1)$, and therefore, the peak-to-peak voltage of v_{TI}, V_{PP_TI}, is expressed as

$$V_{pp\_TI} = \frac{NV_{string} + V_{bus}}{N+1} - \frac{NV_{string}}{N+1} = \frac{V_{bus}}{N+1} \tag{5}$$

The RVM can be equivalently expressed as shown in Fig. 8(a) that allows simplified operation analysis. This equivalent circuit is essentially a series-resonant voltage multiplier driven by a square wave voltage source having a peak-to-peak voltage of V_{pp_TI}. The leakage inductance L_{kg} is reflected on the RVM side, and its inductance value L_{eq} is

$$L_{eq} = \frac{L_{kg}}{(N+1)^2} \tag{6}$$

The characteristic impedance Z_0, characteristic angular frequency ω_0, and resonant angular frequency ω_r are expressed as

$$Z_0 = \sqrt{\frac{L_{eq}}{C_r}},\ \omega_0 = \frac{1}{\sqrt{L_{eq}C_r}},\ \omega_r = \sqrt{\omega_0^2 - \gamma^2} \tag{7}$$

where the damping factor γ is given by

$$\gamma = \frac{R}{2L_{eq}} \tag{8}$$

In this equation, R is the collective resistance of the resonant current path.

Based on the derived equivalent circuit, the detailed analysis and modeling for the RVM are performed. It is noteworthy that theoretical operation waveforms of the equivalent circuit of the RVM are identical to those shown in Fig. 6. The current and voltage of the resonant tank in j-th (j = 1…6) mode, $i_{Cr.j}(t)$ and $v_{Cr.j}(t)$, are expressed as

$$i_{Cr.j}(t) = \frac{V_{TI.j} - V_{Cr.j} - V_{VM.j}}{Z_0} e^{-\gamma(t-T_j)} \sin\omega_r(t-T_j) \tag{9}$$

$$v_{Cr.j}(t) = (V_{TI.j} - V_{VM.j}) - (V_{TI.j} - V_{Cr.j} - V_{VM.j}) e^{-\gamma(t-T_j)} \cos\omega_r(t-T_j) \tag{10}$$

where $V_{TI.j}$ and $V_{VM.j}$ are

$$V_{TI.j} = \begin{cases} \dfrac{V_{bus} + NV_{string}}{N+1} & (j = 1,2,3) \\ \dfrac{NV_{string}}{N+1} & (j = 4,5,6) \end{cases} \tag{11}$$

$$V_{VM.j} = \begin{cases} V_{bias} + (0.5V_i + V_F) & (j = 1,5) \\ V_{bias} - (0.5V_i + V_F) & (j = 2,4) \\ V_{TI.j} - V_{Cr.j} & (j = 3,6) \end{cases} \tag{12}$$

$V_{Cr.j}$ is the $v_{Cr.j}(t)$ at the beginning of j-th mode is

$$V_{Cr.j+1} = v_{Cr.j}(T_{j+1}) = (V_{TI.j} - V_{VM.j}) + (V_{TI.j} - V_{Cr.j} - V_{VM.j}) e^{\frac{-\pi\gamma}{\omega_r}} \tag{13}$$

The average voltage across the TI must be zero under steady-state conditions, and hence, the average voltage of C_r, $V_{Cr.ave}$, is

$$V_{Cr.ave} = \frac{V_{Cr.1} + V_{Cr.3}}{2} = \frac{V_{Cr.2} + V_{Cr.5}}{2} = V_{string} - V_{bias} \tag{14}$$

Substitution of (13) and (14) into (9) produces

$$\begin{cases} i_{Cr.1}(t) = -i_{Cr.4}(t) \\ \quad = \dfrac{e^{-\gamma T_r}}{Z_0(1+e^{-\gamma T_r})} \left\{ \dfrac{V_{bus}}{N+1} + (V_i + 2V_F) e^{\frac{-\gamma T_r}{2}} \right\} \sin\omega_r t \\ i_{Cr.2}(t) = -i_{Cr.5}(t) \\ \quad = \dfrac{e^{-\gamma T_r}}{Z_0(1+e^{-\gamma T_r})} \left\{ -\dfrac{V_{bus}}{N+1} e^{\frac{-\gamma T_r}{2}} + (V_i + 2V_F) \right\} \sin\omega_r t \end{cases} \tag{15}$$

These equations suggest that i_{Cr} is a function of V_i but is not influenced by whether cell voltages are balanced. In other words, the operation of the RVM is not influenced by cell voltage imbalance, as will be demonstrated in Section VII-B.

i_{Cr} is rectified by diodes and is supplied to the least charged cell(s). The rectified i_{Cr}, I_{VM}, is expressed as

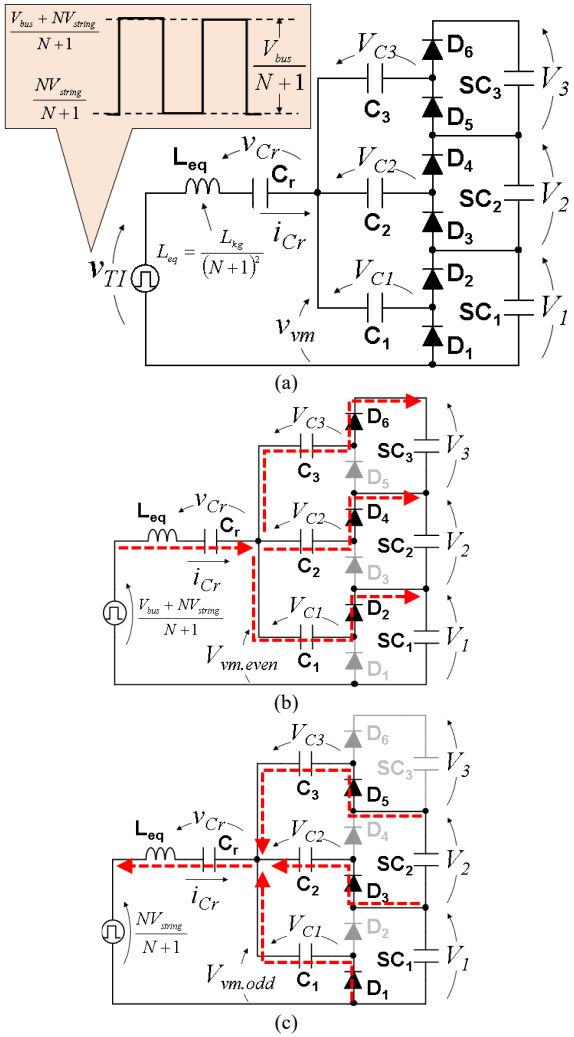

Fig. 8. (a) Equivalent circuit of the resonant voltage multiplier. Current flow paths during (b) even-numbered diodes are on and (c) odd-numbered diodes are on.

$$I_{VM}=\frac{1}{2T_S}\int_0^{T_S}|i_{Cr}(t)|dt = \frac{\omega_S\omega_r}{2\pi Z_0(\gamma^2+\omega_r^2)}\frac{\frac{V_{bus}}{N+1}\left(1+e^{\frac{-\gamma T_r}{2}}\right)^2-V_i(1-e^{-\gamma T_r})}{1+e^{-\gamma T_r}} \quad (16)$$

In the ideal case of $\gamma = 0$ (i.e., $R = 0$), (16) can be simplified as

$$I_{VM}\approx\frac{\omega_S}{\pi Z_0\omega_r}\frac{2V_{bus}}{N+1} \quad (17)$$

This equation indicates that I_{VM} is constant and independent of cell voltage. Hence, currents in the RVM can be automatically limited under the desired value without feedback control, allowing open-loop control for cell voltage equalization.

E. Voltage Equalization Mechanism of Resonant Voltage Multiplier (RVM)

This subsection derives a dc equivalent circuit of the RVM to demonstrate the voltage equalization mechanism. In order to simplify mathematical expressions, the analysis is performed focusing only on voltage values, and the influence of resonant currents is not taken into consideration.

Current flow paths during the even- and odd-numbered diodes are on are shown in Figs. 8(b) and (c), respectively. Voltages of C_1–C_3 during the even-numbered diodes are on, $V_{C1.even}$–$V_{C3.even}$, are given by

$$\begin{cases} V_{C1.even}=V_{VM.even}-(V_1+V_F) \\ V_{C2.even}=V_{VM.even}-(V_1+V_2+V_F) \\ V_{C3.even}=V_{VM.even}-(V_1+V_2+V_3+V_F) \end{cases} \quad (18)$$

where $V_{VM.even} = V_{VM.j}$ (j = 2, 4) [see (12)].

Similarly, voltages of C_1–C_3 during the odd-numbered diodes are on, $V_{C1.odd}$–$V_{C3.odd}$, are expressed as

$$\begin{cases} V_{C1.odd}=V_{VM.odd}+V_F \\ V_{C2.odd}=V_{VM.odd}-(V_1-V_F) \\ V_{C3.odd}=V_{VM.odd}-(V_1+V_2-V_F) \end{cases} \quad (19)$$

where $V_{VM.odd} = V_{VM.j}$ (j = 1, 5) [see (12)].

Voltage variations of C_1–C_3, ΔV_{C1}–ΔV_{C3}, can be yielded from (18) and (19), as

$$\begin{cases} \Delta V_{C1}=V_{VM.even}-V_{VM.odd}-(V_1+2V_F) \\ \Delta V_{C2}=V_{VM.even}-V_{VM.odd}-(V_2+2V_F) \\ \Delta V_{C3}=V_{VM.even}-V_{VM.odd}-(V_3+2V_F) \end{cases} \quad (20)$$

ΔV_{Ci} (i = 1…3) can be expressed in a different way, as

$$\Delta V_{Ci}\propto\frac{I_{eqi}}{C_i f_S}\approx\frac{I_{eqi}}{R_{eqi}} \quad (21)$$

where I_{eqi} is an equalization current supplied to SC_i, C_i is the capacitance, and R_{eqi} is the equivalent resistance of C_i. It should be noted that R_{eqi} in (21) is an approximated value that has been yielded by focusing only on voltage values. The exact value of R_{eqi} is dependent on a current waveform of C_i—for detailed expression, refer to [36]. Substituting (21) into (20) produces

$$V_{VM.even}-V_{VM.odd}=I_{eqi}R_{eqi}+(V_i+2V_F) \quad (22)$$

A dc equivalent circuit of the RVM can be yielded from (22), as shown in Fig. 9. All cells are connected to the secondary winding of an ideal multi-winding transformer through two diodes and one equivalent resistor R_{eqi}. The left- and right-hand sides of (22) correspond to the primary and secondary sides of the transformer. Since the RVM is driven by I_{VM} of (16), the current source I_{VM} is connected to the primary winding.

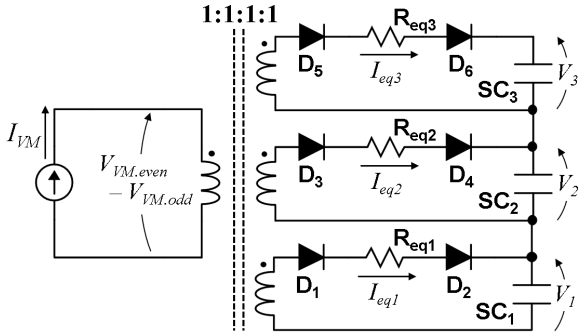

Fig. 9. DC equivalent circuit of resonant voltage multiplier.

I_{VM} on the primary side is reflected to the secondary side in the form of I_{eqi}. Since all the cells are equivalently connected in parallel through respective two diodes and R_{eqi}, I_{eqi} preferentially flows toward the least charged cell having the lowest voltage in the string. Thanks to this current redistribution, a voltage difference between the least charged cell and other cells gradually decreases, and the voltage imbalance will automatically be eliminated.

F. Application of Proposed Integrated Converter to Lithium-Ion Batteries

The proposed integrated converter can possibly be applied to lithium-ion batteries (LIBs), but care must be taken. In general, LIBs require state-of-charge (SOC) equalization rather than voltage equalization. Since a relationship between cell voltage and SOC of SCs is almost linear [37], unifying cell voltages simply can equalize SOCs of SCs. SOCs of LIBs, on the other hand, are nonlinear functions as cell voltage, and therefore, cell voltage equalization of LIBs might exacerbate SOC imbalance.

The RVM in the proposed converter equalizes cell voltages, not SOCs. Hence, in the case of employing the proposed integrated converter for LIBs, careful consideration of whether voltage equalization is acceptable should be taken.

G. Operation in Case of Cell Failures

This subsection discusses the operations of the integrated converter in the case of short-circuit and open-circuit failure modes of SC cells. Images of the short-circuit and open-circuit failure modes are illustrated in Fig. 10, in which the bidirectional PWM converter and RVM in the integrated converter are separately depicted, and smoothing capacitors C_{SC1}–C_{SC3} are not illustrated for the sake of convenience.

An operation image in the case of the short-circuit failure mode of SC_2 is shown in Fig. 10(a). A short-circuit cell can be regarded as a cell with 0 V. The string behaves as a two-cell string, and therefore the bidirectional converter can theoretically charge/discharge the string, though

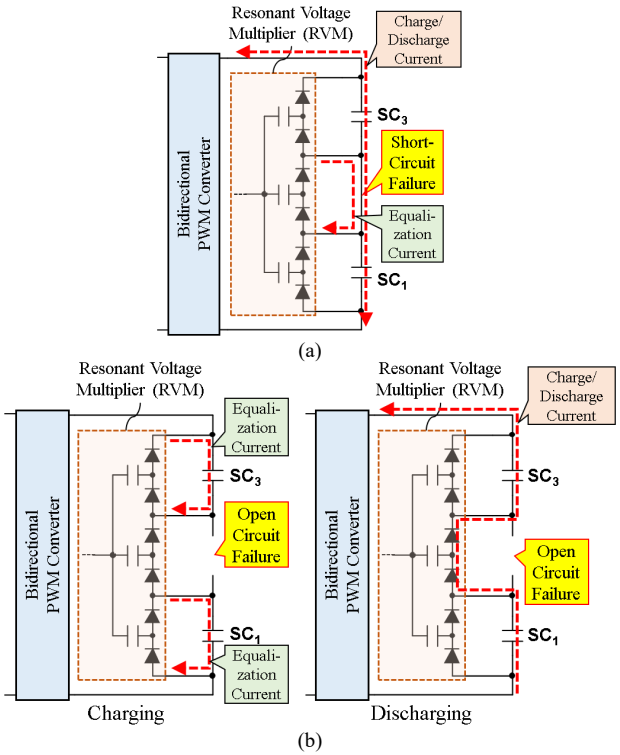

Fig. 10. Operation images in (a) short-circuit failure mode and (b) open-circuit failure mode.

charging/discharging in the short-circuit failure mode is not recommended. An equalization current from the RVM flows toward the short-circuit cell, but no excessive current flows because of the inherent constant current characteristic of the RVM. However, other cells can no longer be equalized because an equalization current always flows toward the short-circuit cell. In summary, the integrated converter can charge/discharge the string, but cells can no longer be equalized in the case of short-circuit failure mode.

An operation in the open-circuit failure mode of SC_2 is shown in Fig. 10(b). Although the PWM converter cannot charge the string because of the existence of the open-circuit cell, other cells still can be charged by equalization currents from the RVM. However, since an equalization current is rather smaller than a charging current, it takes a long time to fully charge the string. As for the discharging process, the string can discharge through diodes in the RVM. Thus, except for the slowed charging process, the integrated converter can operate safely in the open-circuit failure mode.

IV. Design Example of Tapped Inductor

This section presents a design example of a TI of the 100-W prototype for nice cells connected in series. Target specifications include V_{bus} = 48 V and I_{string} = 4.0 A at f_S = 100 kHz (or T_S = 10 μs), and the duty cycle variation range of 0.8 > d > 0.2.

In general, an equalization current necessary to preclude or eliminate voltage imbalance in practical use is reportedly about one-hundredth of charge-discharge currents [39], [40]. In spite of the target specification of I_{string} = 4.0 A, the integrated converter is designed for I_{eq} = 1.0 A at V_i = 2.5 V and V_F = 0.38 in order to expedite the experimental equalization.

A. Resonant Tank

Applying the duty cycle variation range of 0.8 > d > 0.2 into (4) yields f_r, as

$$1-\frac{f_S}{f_r}>0.8,\quad 0.2>\frac{f_S}{f_r}\rightarrow f_r=500\ \text{kHz} \tag{23}$$

In the next step, L_{eq} is determined from (6). In ordinary resonant tanks, ω_r is slightly lower than ω_0 in a practical case. Assuming $\omega_0 = 1.03\omega_r$, γ is yielded from (7), as

$$\omega_r=\sqrt{(1.03\omega_r)^2-\gamma^2}\rightarrow\gamma=7.75\times10^5 \tag{24}$$

To determine L_{eq}, the value of R is necessary. However, a precise value of R is unknown at the design stage. R is the collective resistance in the resonant current path that includes TI's windings, switches, and the RVM containing capacitors and diodes. Resistances of capacitors are in the range of several milliohms, and those of the TI's windings, switches, and diodes are in the range of several ten milliohms. Hence, an estimated R would be around 0.1–0.2 Ω. Assuming R = 0.15 Ω, (6) and (8) yields

$$L_{eq}=\frac{R}{2\gamma}=\frac{0.15}{2\times7.75\times10^5}=0.97\ \mu\text{H} \tag{25}$$

From (7), (24), and (25),

$$C_r=\frac{1}{\omega_0^2L_{eq}}=\frac{1}{(1.03\omega_r)^2L_{eq}}=1.05uF\rightarrow1.0\mu F \tag{26}$$

B. Turn Ratio of Tapped Inductor

In order for i_{Cr} to flow, following boundary conditions, which are obtained from (15), must be satisfied

$$\begin{cases}\dfrac{V_{bus}}{N+1}+(V_i+2V_F)e^{\frac{-\gamma T_r}{2}}>0 & \text{(Modes 1 and 4)}\\ -\dfrac{V_{bus}}{N+1}e^{\frac{-\gamma T_r}{2}}+(V_i+2V_F)<0 & \text{(Modes 2 and 5)}\end{cases} \tag{27}$$

$$\rightarrow N=\frac{N_P}{N_S}<5.78\ \rightarrow\ N=5.5$$

where N_P and N_S are the number of turns of the primary and secondary windings, respectively. Substituting N = 5.5 into (6) yields

$$L_{kg}=L_{eq}(N+1)^2=4.1\ \mu\text{H} \tag{28}$$

C. Magnetizing Inductance of Tapped Inductor

The relationship between an average magnetizing current, I_{Lmg}, and I_{string} is given by (2). The ripple current component of I_{Lmg}, ΔI_{Lmg}, is expressed using a ripple factor β, which is around 0.3 for ordinary PWM converters;

$$\Delta I_{Lmg}=\frac{N+1}{N}\beta I_{string}\rightarrow1.42\ \text{A} \tag{29}$$

In general, for a given output current of an ordinary PWM buck converter (or I_{string} of the proposed integrated converter), a ripple current peaks at d = 0.5. Hence, L_{mg} should be designed to fulfill (29) at d = 0.5 and V_{string} = 24 V.

$$L_{mg} = \frac{\frac{N}{N+1}(V_{bus} - V_{string})dT_S}{\Delta I_{Lmg}} \rightarrow 71.6\,\mu H \quad (30)$$

D. Core Selection

The largest dimension of inductors, $\alpha_{ch.L}$, which can be used as a scaling parameter, is expressed as [41]

$$\alpha_{ch.L} = \left(\frac{S_{tot}}{K_L f \frac{B_{pp}}{2}}\right)^{\frac{1}{\lambda}} \quad (31)$$

where K_L is the coefficient (c.a., 10×10^3), f is the frequency, B_{pp} is the peak-to-peak flux density, and λ is the exponent characterizing the material and shape of the core (c.a., 3.5). S_{tot} is the total volt-amp rating given by

$$S_{tot} = \sum_{All\ Windings} V_{rms} I_{rms} \quad (32)$$

V_{rms} and I_{rms} were obtained from the simulation analysis, and B_{pp} was set to be 100 mT. From the target conditions of V_{string} = 22.5 V, I_{string} = 4.0 A, and I_{eq} = 1.0 A, $\alpha_{ch.L}$ was determined to be 2.41 cm. An RM8 core (PC47RM8Z-12, TDK) with the largest dimension of 2.28 cm was selected.

E. Numbers of Turns of Tapped Inductor

The gap length, l_g, can be determined by the following equation [42].

$$l_g = \frac{\mu_0 L_{mg} I_{max}^2}{B_{max}^2 A_C} 10^4 \text{ [m]} \quad (33)$$

where μ_0 (= $4\pi\times10^{-7}$) is the magnetic permeability, I_{max} (= $I_{Lmg}+\Delta I_{Lmg}/2$) is the maximum current of I_{Lmg}, B_{max} is the maximum flux density, and A_C is the cross-sectional area in cm^2. Applying L_{mg} = 71.6 μH, I_{max} = 5.43 A, B_{max} = 0.25 T, A_C = 0.64 cm^2 [43] yields

$$l_g = \frac{4\pi \times 10^{-7} \times 71.6 \times 10^{-6} \times 5.43^2}{0.25^2 \times 0.64} \times 10^4 = 0.66 \times 10^{-3} \quad (34)$$

According to the date sheet of the core, the A_L value with l_g = 0.66×10^{-3} is 130 nH [43]. The number of turns of the primary winding, N_P, can be calculated as

$$L_{mg} = A_L N_P^2 \rightarrow N_P = \sqrt{\frac{71.6 \times 10^{-6}}{131 \times 10^{-9}}} = 23.3 \quad (35)$$

To satisfy N = 5.5 [see (24)], the turns ratio of the primary to secondary windings, N_P:N_S, can be determined as follows.

$$N_S = \frac{N_P}{N} = \frac{23.3}{5.5} \rightarrow N_P : N_S = 22:4 \quad (36)$$

AWG25 Litz wires were used for both primary and secondary windings. Two and four Litz wires were connected in parallel for the primary and secondary windings, respectively, to reduce winding resistances by filling a bobbin window area.

V. Comparison with Conventional Magnetic Integration Technique and Integrated Converter

A. Comparison with Conventional Magnetic Integration

Magnetic integration techniques for high step-up converters have been proposed in past works [44], [45]. A magnetizing inductance L_{mg} behaves as a boost inductor, and a leakage inductance L_{kg} resonates with a resonant capacitor. Both L_{mg} and L_{kg} are utilized for boost conversion operations in the previous works. Meanwhile, although the TI itself of the proposed integrated converter is essentially identical to that of previous works, L_{mg} and L_{kg} of the TI of the proposed integrated converter are utilized for different purposes, allowing not only the magnetic integration but also the integration of the bidirectional converter and voltage equalizer. Specifically, L_{mg} works as a filter inductor of the bidirectional PWM converter while L_{kg} resonates with C_r to drive the voltage equalizer (i.e., the RVM).

B. Comparison with Conventional Integrated Converter

Both the conventional (see Fig. 2 [36]) and proposed integrated converters offer a simplified system by integrating two converters (i.e., the bidirectional converter and cell equalizer) into a single unit. Series-connected cells can be cycled with equalizing cell voltages by either the conventional or proposed integrated converters. In other words, the functions of the conventional and proposed converters are essentially identical. The major difference is the number of magnetic components necessary in the circuit.

The conventional integrated converter requires not only a filter inductor for the bidirectional converter but also a transformer for the RVM. The transformer in the conventional integrated converter plays two roles of voltage conversion of 1/N and a resonant inductor.

The proposed integrated converter, on the other hand, contains only one magnetic component (i.e., the TI) chiefly because the TI plays three roles—in addition to the voltage conversion (or voltage division) of 1/(N+1), L_{mg} and L_{kg} are utilized as a filter and resonant inductors, respectively. The reduced magnetic component count is a remarkable benefit from the viewpoint of circuit miniaturization.

C. Total Core Volume Comparison with Conventional Integrated Converter

As discussed in Section II, the proposed TI-based integrated converter can halve the number of magnetic components, compared to the conventional one [36] shown in Fig. 2. This section discusses and compares the total core volumes of the proposed and conventional integrated converters.

The largest dimension of inductors $\alpha_{ch.L}$ of the TI in the proposed converter has been determined in Section IV-D [see (31)]. Meanwhile, the largest dimension of transformers, $\alpha_{ch.Tr}$, is expressed as [41]

$$\alpha_{ch.Tr} = \left(\frac{S_{tot}}{K_{Tr}}\right)^{\frac{1}{\lambda}} \quad (37)$$

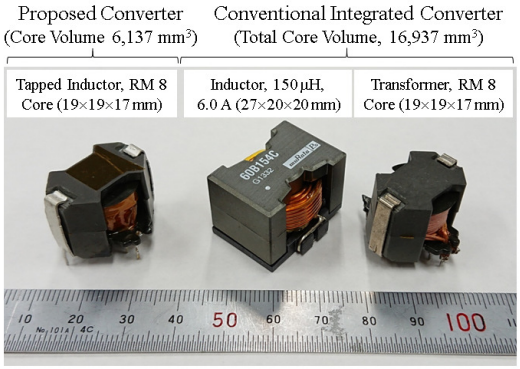

Fig. 11. Actual magnetic components used for proposed converter (Fig. 3) and conventional integrated converter (Fig. 2).

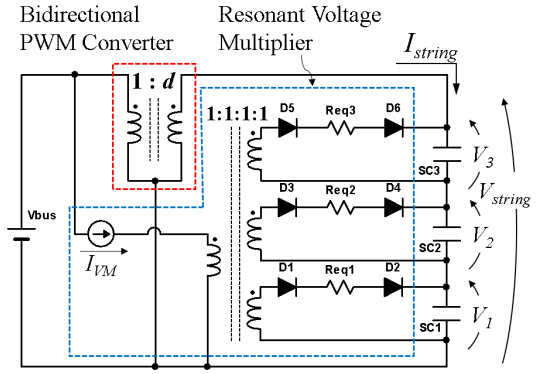

Fig. 12. DC equivalent circuit of integrated converter.

where K_{Tr} is the coefficient (c.a., 15×10^6), and S_{tot} is the total volt-amp rating given by (32).

Applying the same conditions as the integrated converter design (see Section IV-D) yields $\alpha_{ch.L}$ = 2.30 cm and $\alpha_{ch.Tr}$ = 2.19 cm. These calculated values suggest that although the TI requires a larger core (i.e., $\alpha_{ch.L}$ = 2.41 cm, as determined in Section IV-D), the total core volume can be reduced thanks to the reduced magnetic component count.

The actual magnetic components used in the prototypes of the proposed and conventional integrated converters are compared in Fig. 11. The total core volumes of the proposed and conventional integrated converters were 6,127 and 16,937 mm^3, respectively. It should be noted that the inductor for the conventional integrated converter had not been optimized, and hence it is somewhat larger than the optimal one. Similar to the calculation, this photo also indicates the total core volume can be significantly reduced by the TI-based integrated converter.

VI. DC Equivalent Circuit

A. Circuit Description

The dc equivalent circuit of the conventional integrated converter (see Fig. 2) has been derived in [36]. The dc equivalent circuit of the proposed TI-based integrated converter is identical to that of the conventional one, except for the value of I_{VM}.

The dc equivalent circuit for three cells connected in series is shown in Fig. 12. This dc equivalent circuit is the combination of the bidirectional PWM converter that is expressed as an ideal transformer with a turn ratio of 1 : d and the RVM, which has been derived in Section III-E. I_{VM} in the RVM is connected to V_{bus}. The bidirectional PWM converter provides the string with I_{string} for charging/discharging. At the same time, the RVM automatically supplies equalization currents to the least charged cell. During the string is cycled by the bidirectional PWM converter, cell voltages are gradually equalized thanks to this automatic current redistribution by the RVM.

B. Charge-Discharge Cycling

The simulation-based charge-discharge cycling using the dc equivalent circuit was performed for nine cells connected in series. Capacitors, each with a capacitance of 430 F, were used as SC cells, and their initial voltages were intentionally imbalanced. Series-connected SCs were charged with a constant-current–constant-voltage (CC–CV) charging scheme of 1.8 A–22.5 V (2.5 V/cell) for 8 min, followed by 40 W-discharging for 4 min—these conditions are identical to the experiment, as will be shown in Section VII-C. The value of R_{eq} was determined to be 432 mΩ, according to the component values used for the experiment (see Table I) and [36].

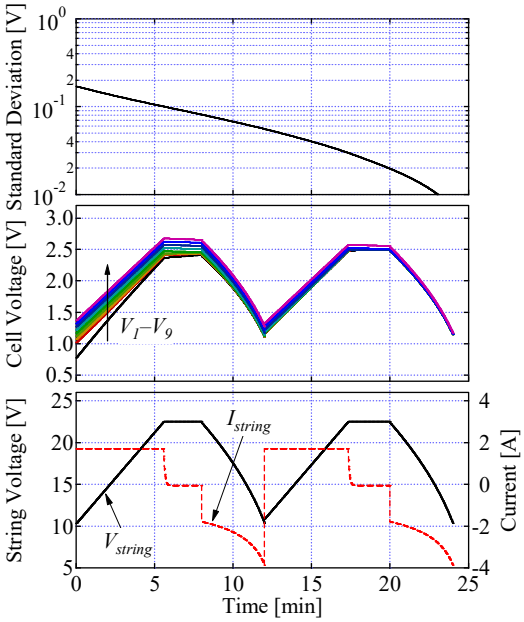

Fig. 13. DC equivalent circuit-based simulation results of charge-discharge cycling for nine cells.

The simulation results are shown in Fig. 13. The voltage imbalance was gradually eliminated during both charging and discharging. Some cells with high initial voltages were over-charged in the first cycle due to the voltage imbalance. In the second cycle, the voltage imbalance became less significant, and all the cells were sufficiently balanced. The standard deviation of cells decreased below 10 mV at the end of the second cycle, adequately eliminating the voltage imbalance.

Note that this simulation analysis was completed in an

instance because the dc equivalent circuit contains no high-frequency switching device. In practice, charge-discharge cycling takes a long stretch of time (several minutes to hours, or even days) compared to switching periods of converters (several microseconds). Such high-frequency simulation for very long hours is impractical from the viewpoints of simulation burden and time. Real-time simulators would accomplish the same task quickly without resorting any circuit simplification, but they cost around several thousand dollars. The analysis based on the derived dc equivalent circuit, on the other hand, can be implemented even with low-end laptop computers. Hence, the dc equivalent circuit is a cost-effective tool to quickly grasp cycling profiles of series-connected cells.

VII. Experimental Results

A. Prototype and Experimental Setup for Individual Characteristic Measurement

A 100-W prototype of the proposed integrated converter for nine SCs was designed and built for the experimental verification, as shown in Fig. 14. Table I lists the components used for the prototype. Conditions of the prototype and experiments are summarized in Table II. For V_{bus} = 48 V and the variation range of V_{string} = 12.6–22.5 V (1.4–2.5 V/cell), the theoretical duty cycle variation range is $0.26 < d < 0.47$. The allowable duty cycle variation range was $0.22 < d < 0.78$, according to (4).

Before performing a charge-discharge cycling test, the fundamental characteristics of the prototype were measured using the experimental setup shown in Fig. 15. In order to measure the individual characteristics of the PWM converter and RVM separately, the output terminal of the integrated converter was separated (see points A and B in Fig. 15). All SCs were removed, and the load resistor R_L and variable resistor R_{var} were used to draw the string current I_{string} and equalization current I_{eq}, respectively. Connecting R_{var} through the tap X emulates the current flow paths in the case that SC_1 is the least charged cell. By selecting the tap Y, on the other hand, the RVM behaves as if all SC voltages are balanced. The voltage of C_{SC1}, V_{Csc1}, corresponds to V_1 (see Fig. 3) in practical use.

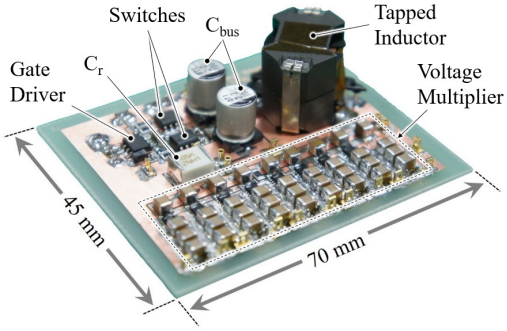

Fig. 14. Photograph of 100-W prototype for nine SCs connected in series.

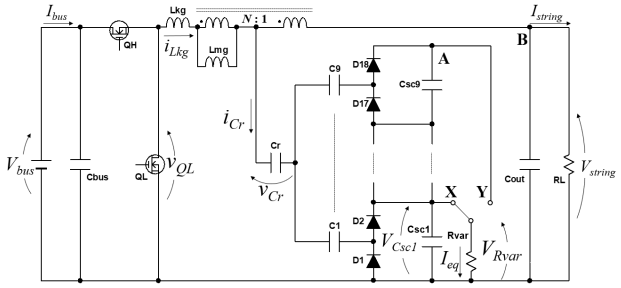

Fig. 15. Experimental setup for waveform and power conversion efficiency measurement.

TABLE I
Component Values

Component	Value
C_{bus}	Aluminum Electrolytic Capacitor, 22 µF × 2
Q_H, Q_L	N-Ch MOSFET, FDS86240, R_{on} = 19.8 mΩ
Tapped Inductor	N_1:N_2 = 22:4, L_{kg} = 4.5 µH, L_{mg} = 71.1 µH RM8 Core (PC47RM8Z-12, TDK)
C_r	Film Capacitor, 1.0 µF
C_1–C_9	Ceramic Capacitor, 47 µF, 35 mΩ
C_{sc1}–C_{sc9}	Ceramic Capacitor, 100 µF × 3
D_1–D_{18}	Dual Schottky Diode, SBE813, V_F = 0.47 V

TABLE II
Conditions of Prototype and Experiment

Converter Power Rating	100 W
Number of SC Cells	9
V_{string}	12.6–22.5 V (1.4–2.5 V/cell)
V_{bus}	48 V
Allowable Variation Range of d	0.22–0.78
f_s	100 kHz
f_r	465 kHz
Maximum I_{eq}	1.0 A
CC–CV Charging	1.8 A–22.5 V (2.5 V/cell)

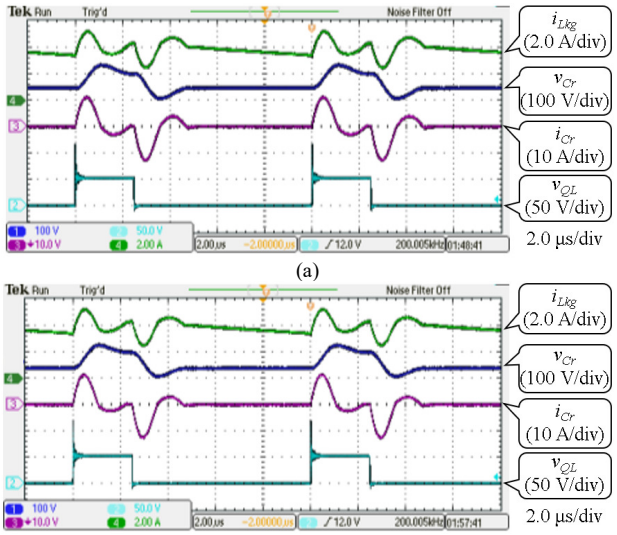

Fig. 16. Measured key waveforms when d = 0.25 and I_{string} = 4.0 A under (a) voltage-balanced condition (I_{eq} ≈ 0.12 A) and (b) voltage-imbalanced condition (I_{eq} ≈ 1.0 A).

B. *Measured Waveforms, Characteristics of RVM, and Power Conversion Efficiency of Integrated Converter*

Measured key operation waveforms when $d = 0.25$ and $I_{string} = 4.0$ A under the voltage-balanced condition ($I_{eq} \approx 0.12$ A) and voltage-imbalanced condition ($I_{eq} \approx 1.0$ A) are shown in Figs. 16(a) and (b), respectively. As the voltage of Q_L, v_{QL}, swung, resonant currents of i_{Cr} flew. Measured waveforms were nearly identical and were unaffected by the voltage-balanced/imbalanced condition. The agreement between the balanced- and imbalanced conditions verified that the resonant operation of the proposed integrated converter was unaffected by whether voltages were balanced or imbalanced, as discussed in Section III-D.

Measured equalization currents I_{eq} and power conversion efficiencies of the RVM under the voltage-balanced and -imbalanced conditions are shown in Figs. 17(a) and (b), respectively. The power conversion efficiency of the RVM, η_{RVM}, is defined as

$$\eta_{RVM} = \frac{V_{Rvar} I_{eq}}{V_{bus} I_{bus}} \times 100 \quad (38)$$

where V_{Rvar} is the voltage of R_{var}, and I_{bus} is the bus current, as designated in Fig. 15.

Under both conditions, the measured characteristics of I_{eq} were nearly constant and independent on d and agreed very well with the theoretical values of (16). The value of I_{eq} under the voltage-imbalanced condition was approximately nine times greater than that under the voltage-balanced condition because currents in the RVM concentrated on SC_1 under the voltage-imbalanced condition.

The measured η_{RVM} was lower than 65%; as the diode forward voltage drop V_F took the significant portion of the V_{SC1}, high-efficiency performance could not be achieved. The measured η_{RVM} monotonically increased with V_{Cac1} as the portion taken by V_F became less significant. A conduction loss of each diode is $I_{eq}V_F$, and eighteen and two diodes conducted in the voltage-balanced and voltage-imbalanced conditions, respectively. The theoretical total diode conduction losses were calculated to be approximately 0.93 W and 0.75 W at $V_{Csc1} = 4.0$ V under the voltage-balanced and -imbalanced conditions, respectively, which accounted for 44% and 36% of the total losses.

Measured power conversion efficiencies of the integrated converter as a whole at various output voltages are shown in Fig. 18. The power conversion efficiency of the integrated

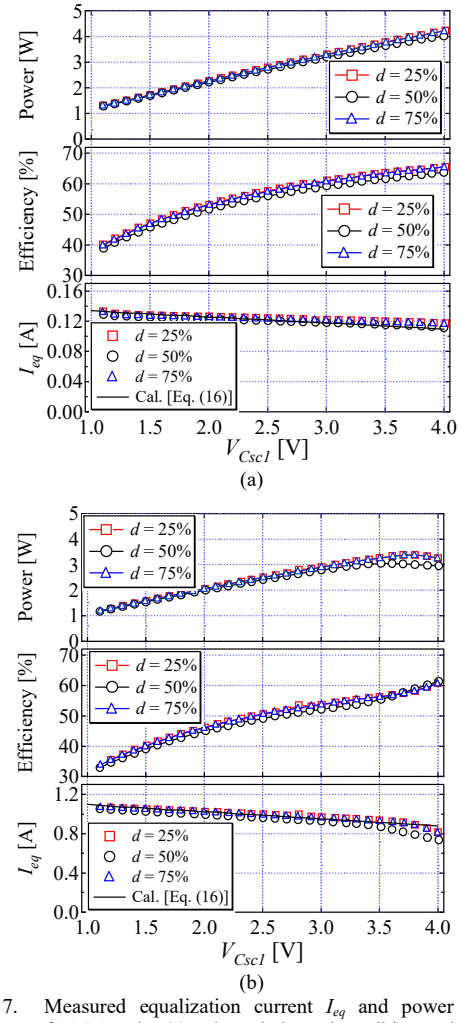

Fig. 17. Measured equalization current I_{eq} and power conversion efficiency of RVM under (a) voltage-balanced condition and (b) voltage-imbalanced condition.

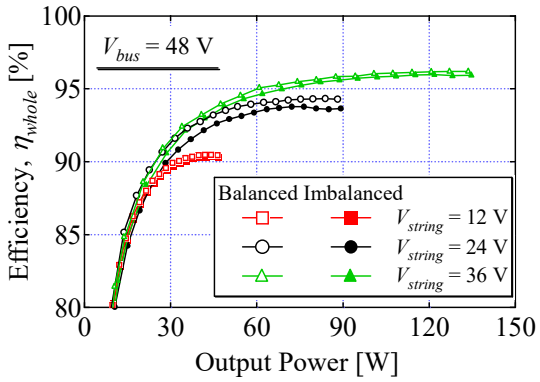

Fig. 18. Measured power conversion efficiencies of integrated converter as a whole under voltage-balanced and -imbalanced conditions.

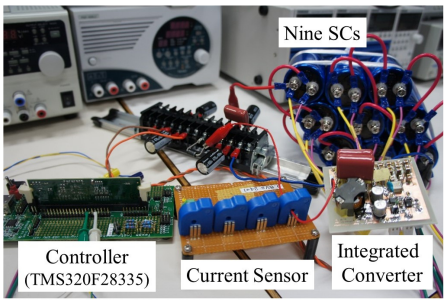

Fig. 19. A photograph of experimental setup for charge-discharge cycling test using integrated converter.

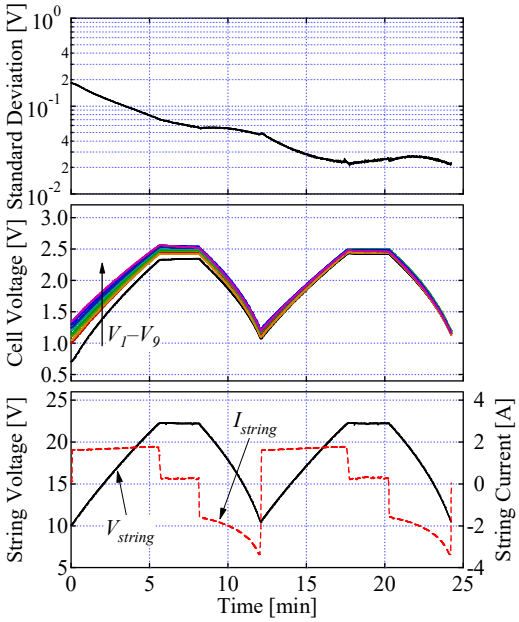

Fig. 20. Resultant charge-discharge cycling profiles of nine SCs connected in series.

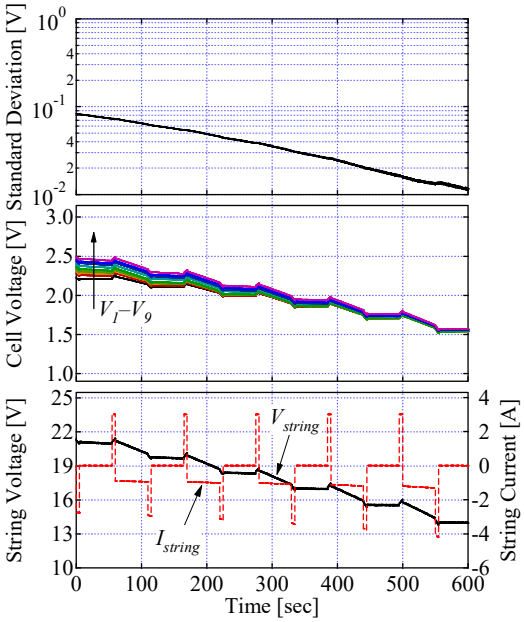

Fig. 21. Resultant profiles of nine SCs connected in series during hybrid pulse power characterization.

TABLE III
INDIVIDUAL CELL VOLTAGES AT BEGINNING AND END OF CYCLING TEST

	Initial	End
V_1	0.698	1.144
V_2	1.001	1.202
V_3	1.051	1.134
V_4	1.107	1.217
V_5	1.150	1.193
V_6	1.203	1.198
V_7	1.251	1.173
V_8	1.300	1.175
V_9	1.349	1.161

TABLE IV
INDIVIDUAL CELL VOLTAGES BEFORE AND AFTER HYBRID PULSE POWER CHARACTERIZATION TEST

	Initial	End
V_1	2.238	1.563
V_2	2.292	1.539
V_3	2.321	1.550
V_4	2.347	1.537
V_5	2.377	1.539
V_6	2.411	1.561
V_7	2.450	1.559
V_8	2.470	1.560
V_9	2.505	1.570

converter as a whole, η_{whole}, is defined as

$$\eta_{whole} = \frac{V_{string} I_{string} + V_{Rvar} I_{eq}}{V_{bus} I_{bus}} \times 100 \qquad (39)$$

where I_{string} is string current.

Although η_{RVM} was lower than 65% as shown in Fig. 17, the measured η_{whole} was higher than 90% in the output power region greater than 30 W. η_{whole} was nearly unaffected by the RVM because the power processed by the RVM was only a fraction of the whole power—the power processed by the RVM was merely 4 W, as can be seen in Fig. 17. The efficiencies under the voltage-imbalanced condition were slightly lower than those under the voltage-balanced condition because of the inferior efficiency characteristics of the RVM under the voltage-imbalanced condition, as shown in Fig. 17(b).

C. Charge-Discharge Cycling Test

The charge-discharge cycling test using the prototype was performed for nine SCs, each with a capacitance of 400 F (the actual capacitance was measured to be approximately 430 F), connected in series. The experimental setup of the cycling test is shown in Fig. 19. Each cycle consisted of CC–CV of 1.8 A–22.5 V (2.5 V/cell) for 8 min and 40 W discharging for 4 min. The initial voltages of SCs were intentionally imbalanced to demonstrate the equalization performance of the prototype.

The resultant charge-discharge cycling profiles are shown in Fig. 20. Individual cell voltages at the beginning and the end of the cycling test are shown in Table III. The voltage imbalance gradually disappeared thanks to the energy redistribution by the RVM. Some cells with high initial voltages were over-charged in the first cycle due to the voltage imbalance. In the second cycle, cell voltage imbalance almost vanished, and all the cells were cycled without being over-charged. The standard deviation of the cell voltages decreased down to 20 mV at the end of the experiment, successfully demonstrating the integrated performance of the proposed converter.

A similar test with dynamic current changes based on the hybrid pulse power characterization [46] was also performed.

The resultant discharging profiles are shown in Fig. 21. Cell voltages before and after the characterization test are shown in Table IV. Thanks to the low impedance nature of SCs, cell and module voltages did not abruptly change in response to dynamic variations in I_{string}. Cell voltage imbalance gradually disappeared even when I_{string} abruptly changed. The standard deviation dropped around 8 mV at the end of the test, verifying the equalization performance of the proposed integrated converter.

VIII. Conclusions

The single-magnetic bidirectional PWM converter integrating the RVM-based voltage equalizer has been proposed for series-connected SCs. The integrated converter is derived from the combination of the bidirectional PWM converter having the TI and RVM. With the proposed concept of integration, the bidirectional converter and voltage equalizer can be integrated into a single unit with reducing the magnetic component count, hence reducing the circuit volume in comparison with the conventional integrated converter.

The experimental charge-discharge cycling test using the 100-W prototype of the proposed integrated converter was performed for nine SCs connected in series. The voltage imbalance gradually disappeared during cycling, demonstrating the integrated functions of the proposed integrated converter.

References

[1] S. Buller, E. Karden, D. Kok, and R.W. De Doncker, "Modeling the dynamic behavior of supercapacitors using impedance spectroscopy," *IEEE Trans. Ind. Appl*., vol. 38, no. 6, pp. 1622–1626, Nov./Dec. 2002.

[2] N. Bertrand, J. Sabatier, O. Briat, and J.M. Vinassa, "Embedded fractional nonlinear supercapacitor model and its parametric estimation method," *IEEE Trans. Ind. Electron*., vol. 57, no. 12, pp. 3991–4000, Sep. 2010.

[3] N. Rizoug, P. Bartholomeus, and P.L. Moigne, "Modeling and characterizing supercapacitors using an online method," *IEEE Trans. Ind. Electron*., vol. 57, no. 12, pp. 3980–3990, Dec. 2010.

[4] A. Hammar, P. Venet, R. Lallemand, G. Coquery, and G. Rojat, "Study of accelerated aging of supercapacitors for transport applications," *IEEE Trans. Ind. Electron*., vol. 57, no. 12, pp. 3972–3979, Dec. 2010.

[5] P.J. Grbovic, P. Delarue, P.L. Moigne, and P. Bartholomeus, "Modeling and control of the ultracapacitor-based regenerative controlled electric drives," *IEEE Trans. Ind. Electron*., vol. 58, no. 8, pp. 3471–3484, Aug. 2010.

[6] J. Moreno, M.E. Ortuzar, and J.W. Dixon, "Energy-management system for a hybrid electric vehicle, using ultracapacitors and neural networks," *IEEE Trans. Ind. Electron*., vol. 53, no. 2, pp. 614–623, Apr. 2006.

[7] A. Allegre, A. Bouscayrol, P. Delarue, P. Barrade, E. Chattot, and S. El-Fassi, "Energy storage system with supercapacitor for an innovative subway," *IEEE Trans. Ind. Electron*., vol. 57, no. 12, pp. 4001–4012, Dec. 2010.

[8] A. Ostadi and M. Kazerani, "A comparative analysis of optimal sizing of battery-only, ultracapacitor-only, and battery–ultracapacitor hybrid energy storage Systems for a city bus," *IEEE Trans. Veh. Technol*., vol. 64, no. 10, pp. 4449–4460, Oct. 2015.

[9] D.B.W. Abeywardana, B. Hredzak, V.G. Agelidis, G.D. Demetriades, "Supercapacitor sizing method for energy-controlled filter-based hybrid energy storage systems," *IEEE Trans. Power Electron*., vol. 32, no. 2, pp. 1626–1637, Feb. 2017.

[10] M. Uno and K. Tanaka, "Accelerated charge-discharge cycling test and cycle life prediction model for supercapacitors in alternative battery applications," *IEEE Trans. Ind. Electron*., vol. 59, no. 12, pp. 4704–4712, Dec. 2012.

[11] S.M. Lambert, V. Pickert, J. Holden, X. He, and W. Li, "Comparison of supercapacitor and lithium-ion capacitor technologies for power electronics applications," in Proc. *Power Electron. Machines and Drives*, 2010, pp. 1–5, Apr. 2010.

[12] M. Uno and K. Tanaka, "Spacecraft electrical power system using lithium-ion capacitors," *IEEE Trans. Aerosp. Electron. Syst*., vol. 49, no. 1, pp. 175–188, Jan. 2013.

[13] Y.S. Lee and M.W. Cheng, "Intelligent control battery equalization for series connected lithium-ion battery strings," *IEEE Trans. Ind. Electron*., vol. 52, no. 5, pp. 1297–1307, Oct. 2005.

[14] P.A. Cassani and S.S. Williamson, "Feasibility analysis of a novel cell equalizer topology for plug-in hybrid electric vehicle energy-storage systems," *IEEE Trans. Veh. Technol*., vol. 58, no. 8, pp. 3938–3946, Oct. 2009.

[15] P.A. Cassani and S.S. Williamson, "Design, testing, and validation of a simplified control scheme for a novel plug-ion hybrid electric vehicle battery cell equalizer," *IEEE Trans. Ind. Electron*., vol. 57, no. 12, pp. 3956–3962, Dec. 2010.

[16] T.H. Phung, A. Collet, and J. Crebier, "An optimized topology for next-to-next balancing of series-connected lithium-ion cells," *IEEE Trans. Power Electron*., vol. 29, no. 9, pp. 4603–4613, Sep. 2014.

[17] A. Baughman and M. Ferdowsi, "Double-tiered switched-capacitor battery charge equalization technique," *IEEE Trans. Ind. Appl*., vol. 55, no. 6, pp. 2277–2285, Jun. 2008.

[18] H.S. Park, C.H. Kim, K.B. Park, G.W. Moon, and J.H. Lee, "Design of a charge equalizer based on battery modularization," *IEEE Trans. Veh. Technol*., vol. 58, no. 7, pp. 3216–3223, Sep. 2009.

[19] M. Uno and K. Tanaka, "Influence of high-frequency charge-discharge cycling induced by cell voltage equalizers on the life performance of lithium-ion cells," *IEEE Trans. Veh. Technol*., vol. 60, no. 4, pp. 1505–1515, May 2011.

[20] Y. Yuanmao, K.W.E. Cheng, and Y.P.B. Yeung, "Zero-current switching switched-capacitor zero-voltage-gap automatic equalization system for series battery string," *IEEE Trans. Power Electron*., vol. 27, no. 7, pp. 3234–3242, Jul. 2012.

[21] M.Y. Kim, C.H. Kim, J.H. Kim, and G.W. Moon, "A chain structure of switched capacitor for improved cell balancing speed of lithium-ion batteries," *IEEE Trans. Ind. Electron*., vol. 61, no. 8, pp. 3989–3999, Aug. 2014.

[22] X. Wang, K.W.E. Cheng, and Y.C. Fong, "Series-parallel switched capacitor balancing circuit for hybrid source package," *IEEE Access*, vol. 6 pp. 34254–34261, Jul. 2018.

[23] Y. Shang, B. Xia, F. Lu, C. Zhang, N. Cui, and C.C. Mi, "A switched-coupling-capacitor equalizer for series-connected battery strings," *IEEE Trans. Power Electron*., vol. 32, no. 10, pp. 7694–7706, Oct. 2017.

[24] K.M. Lee, Y.C. Chung, C.H. Sung, and B. Kang, "Active cell balancing of Li-ion batteries using LC series resonant circuit," *IEEE Trans. Ind. Electron*., vol. 62, no. 9, pp. 5491–5501, Sep. 2015.

[25] K.M. Lee, S.W. Lee, Y.G. Choi, and B. Kang, "Active balancing of Li-ion battery cells using transformer as energy carrier," *IEEE Trans. Ind. Electron*., vol. 64, no. 2. pp. 1251–1257, Feb. 2017.

[26] Y. Shang, C. Zhang, N. Cui, and J.M. Guerrero, "A cell-to-cell battery equalizer with zero-current switching and zero-voltage gap based on quasi-resonant LC converter and boost converter," *IEEE Trans. Power Electron*., vol. 30, no. 7, pp. 3731–3747, Jul. 2015.

[27] F. Baronti, G. Fantechi, R. Roncella, and R. Saletti, "High-efficiency digitally controlled charge equalizer for series-connected cells based on switching converter and upper-capacitor," *IEEE Trans. Ind. Informatics*., vol. 9, no. 2, pp. 1139–1147, May 2013.

[28] N.H. Kutkut, D.M. Divan, and D.W. Novotny, "Charge equalization for series connected battery strings," *IEEE Trans. Ind. Appl*., vol. 31, no. 3, pp. 562–568, May/Jun. 1995.

[29] N.H. Kutkut, H. L.N. Wiegman, D.M. Divan, and D.W. Novotny, "Charge equalization for an electric vehicle battery system," *IEEE Trans. Aerosp. Electron. Syst*., vol. 34, no. 1, pp. 235–246, Jan. 1998.

[30] N.H. Kutkut, H.L.N. Wiegman, D.M. Divan, and D.W. Novotny, "Design considerations for charge equalization of an electric vehicle battery system," *IEEE Trans. Ind. Appl*., vol. 35, no. 1, pp. 28–35, Jan. 1999.

[31] A. Xu, S. Xie, and X. Liu, "Dynamic voltage equalization for series-connected ultracapacitors in EV/HEV applications," *IEEE Trans. Veh. Technol*., vol. 58, no. 8, pp. 3981–3987, Oct. 2009.

[32] M. Arias, J. Sebastian, M.M. Hernando, U. Viscarret, and I. Gil, "Practical application of the wave-trap concept in battery–cell equalizers," *IEEE Trans. Power Electron*., vol. 30, no. 10, pp. 5616–5631, Oct. 2015.

[33] X. Li, J. Xu, S. Xu, F. Qin, S. Zhuang, "Modularised non-isolated two-switch equaliser using full-wave voltage multiplier for series-connected

battery/super-capacitor," *IET Trans. Power Electron*., vol. 12, no. 4, pp. 869–877, Apr. 2019.
[34] M. Uno and K. Tanaka, "Single-switch cell voltage equalizer using multistacked buck–boost converters operating in discontinuous conduction mode for series-connected energy storage cells," *IEEE Trans. Veh. Technol*., vol. 60, no. 8, pp. 3635–3645, Oct. 2011.
[35] M. Uno and A. Kukita, "Double-switch equalizer using parallel- or series-parallel-resonant inverter and voltage multiplier for series-connected supercapacitors," *IEEE Trans. Power Electron*., vol. 29, no. 2, pp. 812–828, Feb. 2014.
[36] M. Uno and A. Kukita, "Bidirectional PWM converter integrating cell voltage equalizer using series-resonant voltage multiplier for series-connected energy storage cells," *IEEE Trans. Power Electron*., vol. 30, no. 6, pp. 3077–3090, Jun. 2015.
[37] TDK. (2010, Sep.) LLC Resonant Power Transformers. [Online]. available: http://www.ic-contract.ru/images/pdf/TDK/e636_srx.pdf#search='TDK+LLC+transforme
[38] M. Uno and A. Kukita, "Cycle life evaluation based on accelerated aging testing for lithium-ion capacitors as alternative to rechargeable batteries," *IEEE Trans. Ind. Electron*., vol. 63, no. 3, pp. 1607–1617, Mar. 2016.
[39] J.W. Kimball, B.T. Kuhn, and P.T. Krein, "Increased performance of battery packs by active equalization," in Proc. *IEEE Veh. Power Propulsion Conf*., pp. 323–327, Sep. 2007.
[40] S. West and P.T. Krein, "Equalization of valve-regulated lead-acid batteries: Issues and life test results," in Proc. *Int. Telecommun. Energy Conf*., pp. 439–446, Sep. 2000.
[41] A.V.D. Bossche and V.C. Valchev, Inductors and Transformers for Power Electronics, New Mexico: CRC Press, 2005, ch.2.1.
[42] R.W. Erickson and D. Maksimovic, Fundamentals of Power Electronics, Switzerland: Springer, 2001, ch.14.
[43] TDK. (2019, Nov.) Ferrite Cores for Switching Power Supplies. [Online]. available: https://product.tdk.com/info/en/catalog/datasheets/ferrite_mz_sw_rm_en.pdf#search='TDK+RM8'
[44] G. Spiazzi, D. Biadene, S. Marconi, and A. Bevilacqua, "Nonisolated high-step-up DC–DC converter with minimum switch voltage stress," *IEEE Trans. Power Electron.*, vol. 34, no. 2, pp. 1470–1480, 2019.
[45] Y. Ye, K.W.E. Cheng, and S. Chen, "A high step-up PWM DC-DC converter with coupled-inductor and resonant switched-capacitor," *IEEE Trans. Power Electron.*, vol. 32, no. 10, pp. 7739–7749, Oct. 2017.
[46] H. Miniguano, A. Barrado, C. Fernández, P. Zumel, and A. Lázaro, "A general parameter identification procedure used for the comparative study of supercapacitors models," *Energies*, vol. 12, no. 9, May 2019, pp. 1–20.

Masatoshi Uno (M'06) was born in Japan in 1979. He received the B.E. degree in electronics engineering and the M.E. degree in electrical engineering from Doshisha University, Kyoto, Japan, and the Ph.D. degree in space and astronautical science from the Graduate University for Advanced Studies, Hayama, Japan, in 2002, 2004, and 2012, respectively.

In 2004, he joined the Japan Aerospace Exploration Agency, Sagamihara, Japan, where he developed spacecraft power systems including battery, photovoltaic, and fuel cell systems. In 2014, he joined the Department of Electrical and Electronics Engineering, Ibaraki University, Ibaraki, Japan, where he is currently an Associate Professor of Electrical Engineering.

His research interests include switching power converters for renewable energy systems, life evaluation for EDLCs and lithium-ion batteries, and development of spacecraft power systems. Dr. Uno received the Isao Takahashi Power Electronics Award in 2018.

Kazuki Yashiro was born in Japan in 1994. He received the B.E. degree and M.E degree in electrical engineering from Ibaraki University, Ibaraki, Japan, in 2016 and 2018, respectively. Since 2018, he has been with Nippon Chemi-Con Corporation.

His research interests include switching power converters and cell voltage equalizers for EDLCs.